#### TURBULENT COHERENT STRUCTURES IN THERMAL VORTEX RINGS

### Paweł JEDREJKO

Faculty of Physics, University of Warsaw, Warsaw, Poland p.jedrejko@uw.edu.pl

The study concerns self-similar structures that emerge during the process of the thermal vortex ring formation. A qualitative explanation of their origin is provided based on the repetitive Kelvin–Helmholtz instability in multiple scales. This phenomenon is found to invert the turbulent energy cascade near the buoyancy interface. To quantify the associated mixing, the fractal dimension of the interface is also computed.

**Keywords:** thermal; vortex; ring; coherent; inverse cascade.



Articles in JTAM are published under Creative Commons Attribution 4.0 International. Unported License https://creativecommons.org/licenses/by/4.0/deed.en. By submitting an article for publication, the authors consent to the grant of the said license.

## 1. Introduction

Thermal vortex rings are an important feature of atmospheric convection. They rise from buoyancy anomalies, i.e., regions of an increased temperature, transporting energy and moisture upwards. In the final stage, they lead to the formation of cumulus clouds (Yano, 2023).

Due to the very wide range of scales in the atmosphere, thermals are usually left unresolved in numerical weather prediction. However, they are used as conceptual building blocks of subgrid-scale, convective phenomena which have to be modeled. For that reason, features of thermals' dynamics are of high interest and remain an active field of study (Morrison *et al.*, 2023; Yano & Morrison, 2024).

A particularly significant aspect of the dynamics of an isolated thermal is its entrainment rate (Morrison et al., 2023). This problem is directly connected to the features of near-interface turbulence. Being affected by the updraft and the ring formation, turbulence there is hardly homogenous, isotropic, and statistically steady. A promising approach is to focus on its persisting, case-dependent features and symptoms of self-organization. These could be understood as effects of underlying coherent structures whose dynamics locally dominate the flow.

In this article, we study the early stages of the evolution of the vortex ring. The main focus is on understanding the formation of coherent structures which emerge during the ring formation. The setup of the problem is the same as described in (Jędrejko *et al.*, 2024). However, while (Jędrejko *et al.*, 2024) focuses on the methodology and numerics, the work presented below is devoted to the interpretation of physical phenomena.

The main outcome of the article is a phenomenological explanation of a local inversion of the energy cascade in the proximity of a convective structure. This goal justifies the methodology chosen and makes a novel contribution to the studies of atmospheric turbulence.

Section 2 briefly presents the problem and crucial assumptions to make the article comprehensive. Next, Section 3 shows an outline of the ring evolution to provide a physical context for the study of coherent structures. Section 4 justifies some useful simplifications that allow the dynamics to be conceptually understood. Further sections describe the coherent structures, the associated energy transfer, and mixing processes. The latter is done by determining the fractal dimension of the anomaly's interface.

#### 2. Problem statement

The problem under consideration is the evolution of an axisymmetric, buoyancy anomaly (Fig. 1). The focus is on the early stages of the process, which justifies the assumption of azimuthal symmetry, according to Yano and Morrison (2024). The anomaly consists of a region of uniform, increased temperature  $T_0$ , which is related to buoyancy by the Boussinesq approximation:

$$\mathbf{b} = -\mathbf{g}\beta(T - T_{\infty}),\tag{2.1}$$

where  $\beta$  is the thermal expansion coefficient and  $T_{\infty}$  is the reference ambient temperature. The change in buoyancy is assumed to be discontinuous and its shape is initialized as a sphere using cylindrical coordinates  $\{\rho, \phi, z\}$ :

$$\mathbf{b}(\mathbf{r}, t = 0) = \begin{cases} b_0 \widehat{z}, & |\mathbf{r}| \le R, \\ \mathbf{0}, & |\mathbf{r}| > R, \end{cases}$$
 (2.2)

with  $b_0 = g\alpha(T_0 - T_\infty)$ . The system starts to evolve from rest, i.e.,  $\mathbf{u}(\mathbf{r}, t = 0) = \mathbf{0}$ .

Typical scales of atmospheric thermals can be estimated from (Sherwood *et al.*, 2013), which reports  $R \approx 10^3$  [m] and  $b_0 \approx 10^{-2}$  [m/s<sup>2</sup>]. Together with the air's thermal ( $\alpha$ ) and momentum ( $\nu$ ) diffusivities  $\approx 10^{-5}$  [m/s<sup>2</sup>], this results in huge Reynolds and Peclet numbers:

$$Re = \frac{\sqrt{R b_0} R}{\nu} \approx 10^{10}, \qquad Pe = \frac{\sqrt{R b_0} R}{\alpha} \approx 10^{10}$$
 (2.3)

(Morrison et al. (2023) refers to Re  $\approx 10^9$ ). For that reason, all diffusive processes are neglected. This assumption implies that the buoyancy distribution remains discontinuous and the sharp interface bounding the anomaly can be tracked in Lagrangian fashion:

$$\mathbf{r}(\xi,t) = \begin{bmatrix} \rho(\xi,t) \\ z(\xi,t) \end{bmatrix}, \qquad \xi \in [-\pi/2,\pi/2)$$
(2.4)

with the initial condition (Fig. 1a) of

$$\mathbf{r}(\xi, t = 0) = R \begin{bmatrix} \sin(\xi) \\ \cos(\xi) \end{bmatrix}. \tag{2.5}$$

Note that the shape of the interface (Eq. (2.4)) does not depend on  $\phi$  due to the symmetry assumed.

The evolution of buoyancy distribution is governed by a simple advection equation:

$$\frac{D\mathbf{b}}{Dt} = 0. ag{2.6}$$

Using the vorticity equation:

$$\frac{D\omega}{Dt} = (\omega \cdot \nabla)\mathbf{u} + \nabla \times \mathbf{b},\tag{2.7}$$

it can easily be noted that the anomaly's interface coincides with a vortex sheet. This is because the source term  $\nabla \times \mathbf{b}$  gives  $\mathbf{0}$  in regions of uniform  $\mathbf{b}$ , and singularity at the discontinuity. By introducing the vortex sheet strength  $\gamma$ :

$$\gamma(\xi, t) \, \mathrm{d}\xi = \omega \, \mathrm{d}r \, \mathrm{d}z,\tag{2.8}$$

the vorticity equation is reduced to:

$$\frac{\mathrm{d}\gamma}{\mathrm{d}t} = b_0 \frac{\partial z}{\partial \xi}.\tag{2.9}$$

The system is further solved numerically, as described in detail in (Jędrejko et al., 2024), by discretizing the vortex sheet with a set of nodes and segments connecting the nodes. The time integration is done by an adaptive 4th-order Runge–Kutta scheme. The spatial derivative in Eq. (2.9) is computed with the 2nd-order central difference, and the integral (Eq. (2.10)) with the trapezoidal rule. The latter two allow more flexibility in the adaptive discretization of the sheet than higher-order schemes. Such a procedure is necessary to keep the resolution fine, by splitting segments, which got too long.

An important part of the method is also the regularization of the Biot-Savart kernel, introduced by Krasny (1986) and Nitsche and Krasny (1994):

$$\mathbf{u}_0 = \int_0^{2\pi} \int_{-\pi/2}^{\pi/2} \frac{\gamma \widehat{\phi} \times (\mathbf{r}_0 - \mathbf{r})}{(|\mathbf{r}_0 - \mathbf{r}|^2 + \delta^2)^{3/2}} \rho \, \mathrm{d}\xi \, \mathrm{d}\phi.$$
 (2.10)

It can conceptually be understood as assigning some finite thickness  $\delta$  to the vortex sheet. As a result, dumping is applied to the highest wavenumbers of the velocity field induced. The main consequence is the bound on the smallest scales present in the flow, especially the smallest wavelengths of the vortex sheet instabilities. The qualitative evolution of the process remains the same, although the rising speed of the thermal is affected. However, this influence is weak (<5% for  $\delta \in [0.004,\ 0.016]$ ) and separate from the interscale energy transfer. As can be deduced from Eq. (2.10), the impact of  $\delta$  is mainly local.

Alternative approaches to regularization can also be found in the literature (comparison might be found in (Sohn, 2014)), although no discrepancies, significant for this study, are reported. The advantage of the regularization type chosen is its simplicity. This allows us to take the azimuthal integral analytically and use some algorithmic optimizations (like Dynnikova (2009)), described in detail in (Jędrejko et al., 2024).

# 3. Outline of the system evolution

In the initial stage, the anomaly experiences rapid collapse at the bottom, which transforms the initial sphere to the final vortex ring. Meanwhile, the vortex sheet at the sides is dominated by a series of coherent vortices, which are the main focus of this article. As time passes, the vortices get larger and fill the "interior" of the anomaly with the vortex sheet. This is done by intensive stretching and folding. Figure 1 presents successive stages of the ring's evolution. The subfigure (a) captures the initial condition, (b) the beginning of the collapse with coherent vortices on the side, and (c) the beginning of the ring's closure and space-filling interface.

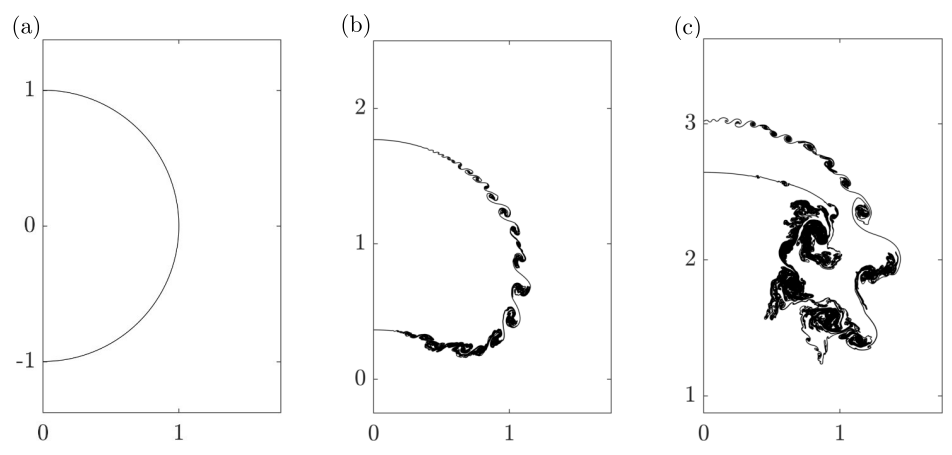


Fig. 1. Evolution of the interfacial vortex sheet in selected time steps: (a) t = 0; (b)  $t \approx 1.5$ ; (c)  $t \approx 3$ . Obtained with  $\delta = 0.008$ .

## 4. An analogy to Kelvin-Helmholtz instability

The vortex sheet strength is initially amplified at the sides by the buoyancy (2.9), which launches two concurrent processes (Fig. 1b). The first is the anomaly collapse at the bottom, which ultimately turns it into a vortex ring. The second takes place at the sides and leads to the formation of coherent vortices exhibiting some self-similarity features.

In this section, we will argue that the latter can be qualitatively understood in analogy to the classical Kelvin–Helmholtz (K-H) instability. By that, we mean the case of the plane, periodic vortex sheet, with constant strength  $\gamma$  and finite thickness  $\delta$ . Such a sheet experiences a rollup when perturbed (Vallis, 2006 [chapter 6.2.4]; Krasny, 1986), giving rise to the characteristic "cat-eve" vortices.

The circumstances of vortex formation considered in this article differ from the classical K-H by a few features. The vortex sheet is curved, its strength is dynamically changed by buoyancy, and the simultaneous collapse exerts stretching. However, we will argue in favor of a scale separation, which leaves the coherent vortices relatively unaffected by these aspects.

The characteristic length of the initial K-H vortices is  $\delta$  from Eq. (2.10), which is shown in (Krasny, 1986). That reference discusses perturbations in the form of:

$$x = Xe^{\sigma t + ik\gamma\xi}, \qquad y = Ye^{\sigma t + ik\gamma\xi},$$
 (4.1)

where  $\{x,y\}$  are Cartesian coordinates describing the shape of the vortex sheet, X, Y are constant, initial amplitudes and  $k = 2\pi/\lambda$  is the wavenumber. The analysis leads to the relation:

$$\sigma^2 = \frac{k(1 - e^{-k\cosh^{-1}(1+\delta^2)})e^{-k\cosh^{-1}(1+\delta^2)}}{4\delta(2+\delta^2)^{1/2}},\tag{4.2}$$

which we use to numerically obtain the fastest-growing wavelength  $\Lambda$  as a function of  $\delta$ . The resulting relation seems to be linear as shown in Fig. 2 and by regression found to be:

$$\Lambda(\delta) = \alpha \delta, \qquad \alpha = 6.1445. \tag{4.3}$$

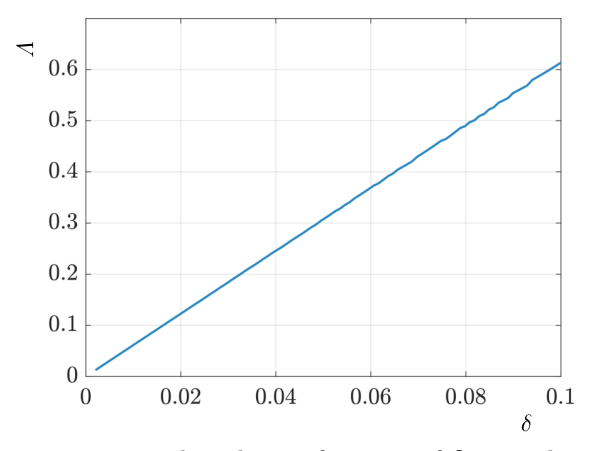


Fig. 2. Fastest growing wavelength as a function of  $\delta$ , according to Eq. (4.2).

The values of  $\delta$  considered are much smaller than the anomaly radius:

$$\frac{\delta}{R} \ll 1,\tag{4.4}$$

thus we assume that the curvature of the vortex sheet does not affect the formation of K-H vortices much.

The characteristic time of the anomaly bulk evolution is independent of  $\delta$ , as shown in (Jędrejko *et al.*, 2024) and can be expressed by

$$t_b = \sqrt{\frac{R}{b_0}}. (4.5)$$

The characteristic time of local  $\gamma$  amplification (Eq. (2.9)) depends on the local shape. Thus, it is  $t_b$  before the instability and

$$t_{\gamma} = \sqrt{\frac{\delta}{b_0}} \tag{4.6}$$

afterward. The cat-eye eddy turn-over time is

$$t_{\delta} = \frac{\delta^2}{\gamma} = \frac{\delta^2}{b_0 R t_b} = \frac{\delta^2}{\sqrt{b_0 R^3}},\tag{4.7}$$

where we used Eq. (2.9) to determine the accumulation of  $\gamma$  till the emergence of K-H eddies. This happens in time  $t_b$  in the condition of local shape characterized by R.

As the first outcome:

$$\frac{t_{\delta}}{t_{\gamma}} = \left(\frac{\delta}{R}\right)^{3/2} \ll 1,\tag{4.8}$$

so it is expected that  $\partial \gamma/\partial t$  is of secondary importance for the evolution of K-H vortices at the sides of the anomaly.

This result was also checked numerically by running a separate simulation with  $\gamma$  fixed in time:

$$\gamma_0 = b_0 \cos(\xi),\tag{4.9}$$

which is an initial tendency of  $\gamma(\xi,t)$ , deduced from Eqs. (2.9) and (2.5). The comparison is presented in Fig. 3 for the snapshots, where the anomaly center is at the same height. This happens for  $t \approx 0.56$  for the constant  $\gamma_0$  and  $t \approx 0.89$  for dynamic  $\gamma$ . The time shift is due to the fact that in the latter case,  $\gamma$  has to be amplified in time to reach the value of  $\gamma_0$ . This happens mostly "in place", because the initial  $\gamma$  is too weak to significantly change the state of the system. However, the tiny progress of the anomaly's collapse in the initial period results in a small difference in its thickness along the vertical axis (Fig. 3a). Despite these differences in the bulk evolution and the resulting "rigid-body" translation of the K-H vortices, their shapes are

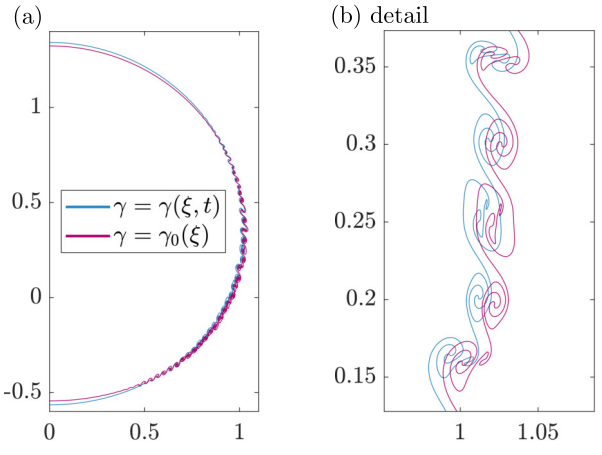


Fig. 3. Comparison of the case with  $\gamma$  evolving according to Eq. (2.9) and the case with  $\gamma$  fixed at the initial tendency. Anomalies centered at the same point.

de facto indistinguishable (Fig. 3b). Therefore, the time dependence of  $\gamma$  is insignificant for the evolution of K-H vortices.

The second outcome from the dimensional analysis is

$$\frac{t_{\delta}}{t_{b}} = \left(\frac{\delta}{R}\right)^{2} \ll 1,\tag{4.10}$$

so the collapse and the initial cat-eye vortices have well-separated time scales.

Knowing already that the sheet curvature (Eq. (4.4)) and  $\partial \gamma / \partial t$  (Eq. (4.8)) are negligible for K-H, an a posteriori argument for the collapse and K-H separation is the accuracy of Eq. (4.3). For  $\delta = 0.008$  it predicts  $\Lambda = 0.04916$  and, as shown in Fig. 5, despite the collapse we get  $\Lambda = 0.04908$ .

In summary, Eqs. (4.4), (4.8), (4.10) justify the reasoning based on the classical K-H instability in understanding the coherent structures at the sides of the anomaly.

### 5. The concept of hierarchical Kelvin–Helmholtz instability

The most interesting feature of the coherent structures on the sides of the anomaly is their self-similarity. We explain it by referring to the idea of hierarchical instability.

First, K-H instability occurs, and the vortex sheet gets covered with a layer of cat-eye vortices. Their size is determined by the sheet thickness  $\delta$  as given by Eq. (4.3). Such a layer effectively starts to behave like a new, thicker vortex sheet. Because it is built of smaller structures, its effective strength is initially perturbed. This leads to the new K-H instability in higher wavelengths due to higher effective thickness. The process repeats, with each new generation of vortices approximately doubling the characteristic wavelength of the previous one. This proceeds till the value of effective  $\delta$  breaks the condition (4.4), then (4.8) and (4.10), which couples the dynamics of the structures with other processes in the system.

This interpretation is justified by running the case with twice the higher value of  $\delta$ . The resulting vortices are very similar to the second generation of vortices from the case with lower  $\delta$ , see Fig. 5. Both systems further evolve analogically, doubling the characteristic size of the structures in an iterative manner. This phenomenon naturally raises a question about the local inverse energy cascade.

# 6. Energy transfer by the hierarchical K-H

The investigation of the energy transfer associated with the structures described in the previous section is troublesome. The two-dimensional Fourier transform would have to be bounded to a finite, non-periodic domain. It is also highly affected by the updraft in the center of the anomaly. To analyze the energy of the interfacial structures exclusively, we turn to different methodology based on an FFT along the contour.

#### 6.1. Generation renewal

The vortex sheet is parametrized with its initial length, as in Eq. (2.4). Note that although the formation of a single cat-eye vortex stretches the sheet very intensively, it takes place in a fixed range of  $\xi$ .

As long as the overall shape of the anomaly was not affected much by the collapse (say t < 1.5, compare with Fig. 1), this range is a good measure of the vortex size. This is because it corresponds to the length of that interface piece at the reference stage, i.e., before the roll-up (Fig. 4).

This approach also holds for the next generations of vortices, as long as the collapse does not proceed too far. For that reason, a Fourier transform of functions of  $\xi$  provides an insight



Fig. 4. Conceptual drawing of a material piece of the interface before (light) and after (dark) the roll-up. Its initial length  $(\xi_2 - \xi_1)$  is a good measure of the eddy size.

into eddy scale distribution. This is especially convenient because an interface, as a closed loop, is periodic. Fortunately, scales of the anomaly collapse and K-H (in the initial stage) are well separated. We use a threshold of  $\lambda=0.5$  and interpret the most energetic wavelength below it as a characteristic scale of the K-H. Figure 5 presents a dominant K-H scale as a function of time for three values of  $\delta$ .

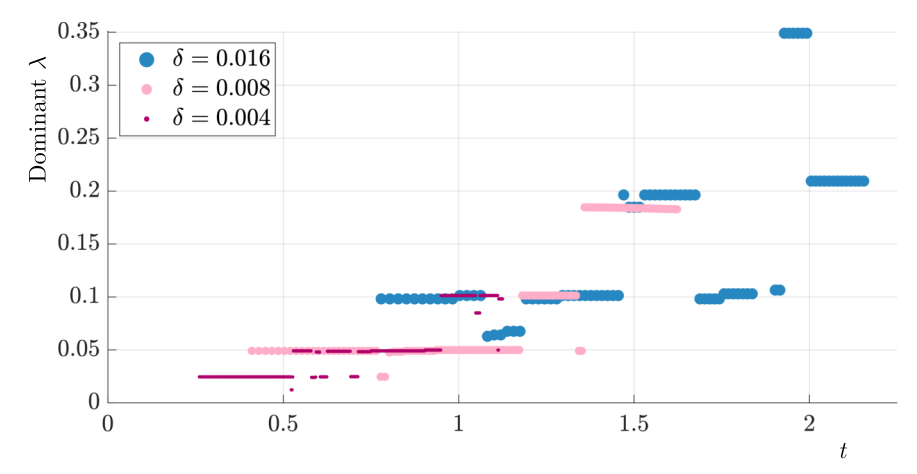


Fig. 5. Most energetic wavelengths (among shorter than 0.5) in time show distinct generations of vortices.

The instability seems to develop later for higher  $\delta$ , but this can be caused by the details of discretization applied to each case. What is worth noting is a clear generation renewal with size doubling, leading to the shift of energy towards large wavelengths. Moreover, the second generation for  $\delta$  closely matches the scale of the first generation for  $2\delta$ . In further times t > 1.5, the size doubling is less exact. This might be caused by the collapse, which makes the initial condition no longer a good reference point, or by breaking conditions (4.4), (4.8), (4.10). At some stages, the competition between current and previous generations is close, leading to a temporal jump-back of the dominant  $\lambda$ . This indicates that a new generation is built on top of the previous one rather than instead of it. Figure 5 is also in good agreement with Eq. (4.3), which is presented in Table 1.

Table 1. Wavelengths of subsequent generations (Fig. 5) compared with predictions of Eq. (4.3).

δ	Generation 1 (Eq. (4.3))	Generation 1	Generation 2	Generation 3
0.004	0.02458	0.02454	0.04909	0.10134
0.008	0.04915	0.04908	0.10139	0.18467
0.016	0.09831	0.09820	0.19635	0.34907

# 6.2. Spectrum along the smoothed contour

An alternative approach for the energy transfer analysis is to sample the velocity along a smoothed contour and then compute its Fourier transform. This is more computationally demanding but is not limited to the early stages of the system evolution.

A separate simulation with high  $\delta=0.1$  is used to obtain a smooth contour. Because a significant range of small scales is dumped, the rising and collapse speeds are affected. For that reason, a case with  $\delta=0.1$  at time t does not fit the case  $\delta=0.008$  at t very well. However, if the thickness of the ring (along the z-axis) is matched and the height is adjusted, two contours match closely (example in Fig. 6).



Fig. 6. Smoothed contour ( $\delta = 0.1$ ) in black, in front of the  $\delta = 0.008$  interface (gray). Contours associated with the thickness at z-axis. Shifting along z applied to match the heights.

Spectra of low- $\delta$  sheet's kinetic energy, computed along high- $\delta$  contours, are presented in Fig. 7. The system accumulates energy over time. Therefore, to compare its various stages, plots were normalized with K-H peak energy. Figure 8 includes examples of the flow structures as a reference. The results from Fig. 7 are in good agreement with outcomes from the previous subsection, shown in Fig. 5. They both indicate a transfer of energy towards larger scales. The characteristic wavelengths are also consistent with what can be noted with the naked eye (Fig. 8). This applies to both their size and complexity, which is related to the width of a given peak from Fig. 7.

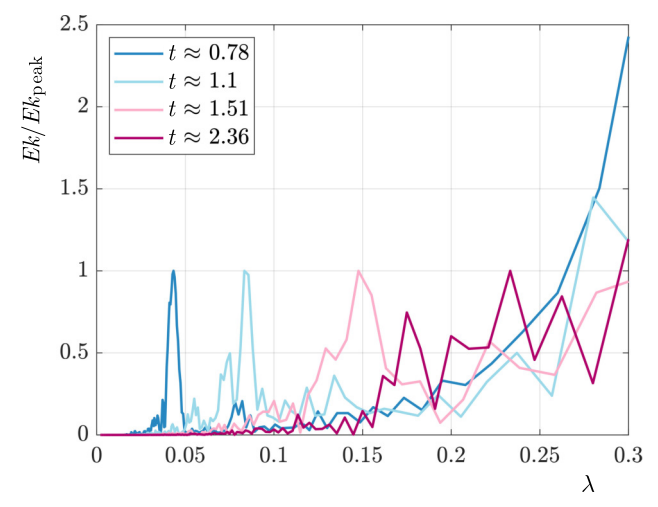


Fig. 7. Normalized energy spectra for selected timesteps. Results obtained with  $\delta=0.008$ . Presented wavelength range associated with K-H instability.

## 7. Fractal dimension of the hierarchical K-H

The intense stretching and folding associated with the hierarchical K-H tightly fills the space with the vortex sheet. The phenomenon is similar in nature to the classical Smale's horseshoe map (Shub, 2005). To measure the intensity of mixing associated with this process, we determine the time evolution of the interface fractal dimension. This is done with the box-counting method

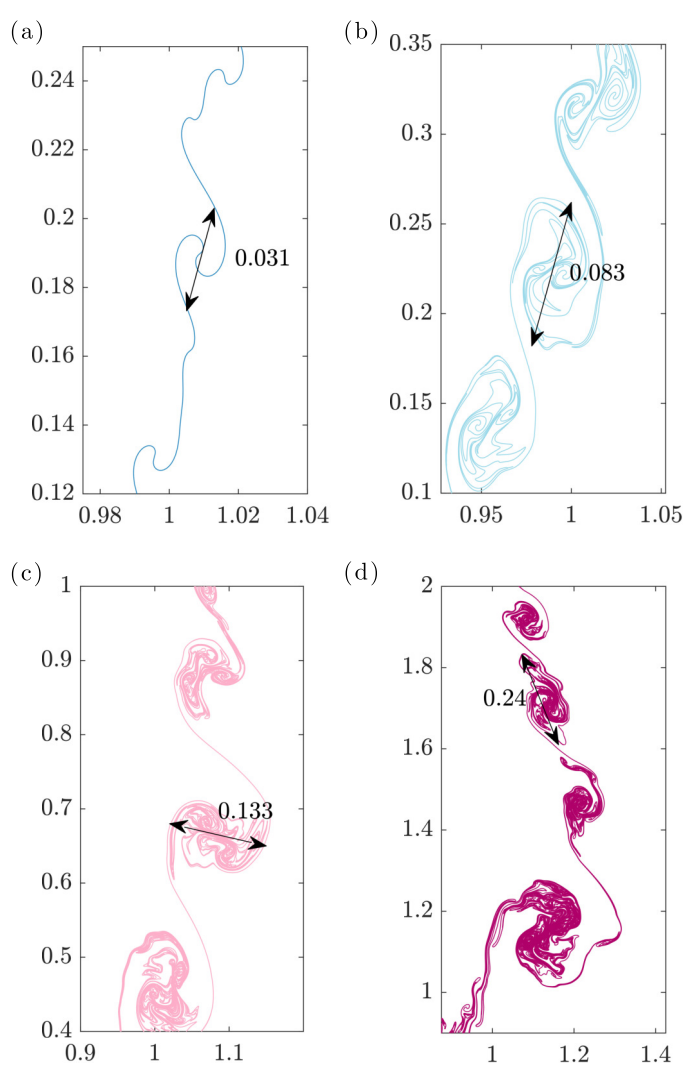


Fig. 8. Approximated characteristic scales of proceeding generations of K-H vortices,  $\delta = 0.008$ : (a)  $t \approx 0.78$ ; (b)  $t \approx 1.10$ ; (c)  $t \approx 1.51$ ; (d)  $t \approx 2.36$ . Colors matched with Fig. 7.

(Liebovitch & Toth, 1989). For that purpose, the domain is covered with a uniform grid of spacing (i.e., box side) d. Then, boxes crossed by the vortex sheet are counted, giving a total number of n(d). The process is repeated for a range of box sizes d, and the fractal dimension is evaluated using Minkowski–Bouligand definition (Bishop & Peres, 2017):

$$D_{\text{box}} = \lim_{d \to 0} \frac{\log(n)}{\log(1/d)},\tag{7.1}$$

which implies:

$$n(d) \approx C d^{-D_{\text{box}}}.$$
 (7.2)

The scaling of Eq. (7.2) for example timesteps is presented in Fig. 9a. The time evolution of the fractal dimension is shown in Fig. 9b.

The evaluated fractal dimension experiences rapid growth when the hierarchical K-H starts and converges to about 1.78. This exceeds the range of 1.3–1.66 found in cloud interfaces (Malinowski & Zawadzki, 1993). This could be an artifact of axial symmetry, which is less and less justified in later times. The first notable plateau in the fractal dimension (Fig. 9b) is at the level of 1.6, so inside the typical cloud range.

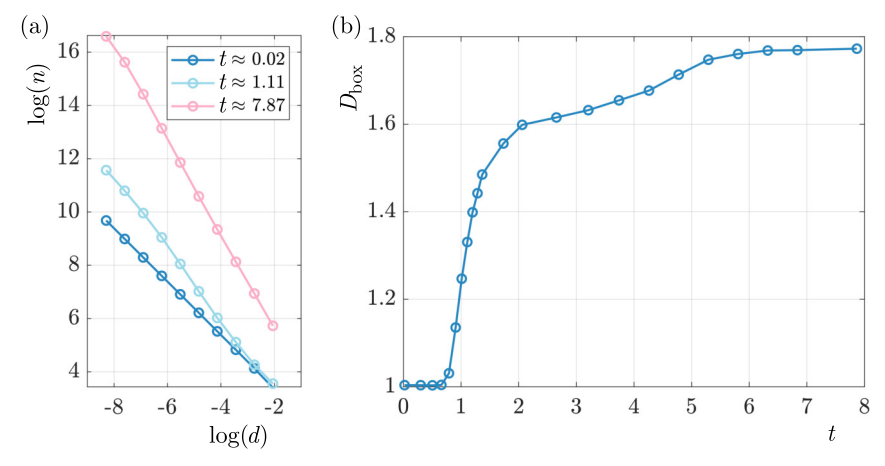


Fig. 9. (a) Number of boxes vs box size; (b) box counting dimension in time.

## 8. Summary and discussion

In this study, we investigated the coherent structures that emerge in the initial stages of the thermal vortex ring formation. Its self-similar nature was explained in analogy to the K-H instability, which occurs multiple times in increasing wavelengths. A related, subsequent stretching and folding introduce intense mixing. This is manifested as an increase in the interface's fractal dimension, growing up to about 1.78.

This hierarchical K-H instability was also found to locally transfer energy to large scales. Such behavior is characteristic of two-dimensional turbulence (Davidson, 2015, chapter 10) and, for late times, could be an artifact of axial symmetry. However, the time range considered in this paper is definitely within the range of physically justified axial symmetry, according to (Yano & Morrison, 2024). The initial inversion of the turbulent cascade near the interface is, therefore, trustworthy. The important question is how long such an inverse cascade remains active. The problem of its azimuthal stability and interaction with long-term stretching is left for further study.

## Acknowledgments

The oral presentation of this work was awarded 2nd place in the Janusz W. Elsner Competition at the 26th Fluid Mechanics Conference in Warsaw (2024). The author gratefully acknowledges the Organizing Committee for recommending this manuscript and covering the publication fee.

## References

- 1. Bishop, C.J., & Peres, Y. (2017). Fractals in probability and analysis. Cambridge Studies in Advanced Mathematics, vol. 162. Cambridge University Press.
- 2. Davidson, P.A. (2015). Turbulence: An introduction for scientists and engineers (2nd ed.). Oxford University Press.
- 3. Dynnikova, G.Ya. (2009). Fast technique for solving the N-body problem in flow simulation by vortex methods. Computational Mathematics and Mathematical Physics, 49(8), 1389-1396. https://doi.org/10.1134/S0965542509080090
- 4. Jędrejko, P., Yano, J.-I., & Wacławczyk, M. (2024). A Lagrangian approach to thermal vortex rings simulation in high Re and high Pe limit. Under consideration in Theoretical and Computational Fluid Dynamics.
- 5. Krasny, R. (1986). Desingularization of periodic vortex sheet roll-up. *Journal of Computational Physics*, 65(2), 292–313. https://doi.org/10.1016/0021-9991(86)90210-X

- 6. Liebovitch, L.S., & Tibor, T. (1989). A fast algorithm to determine fractal dimensions by box counting. *Physics Letters A*, 141(8–9), 386–390. https://doi.org/10.1016/0375-9601(89)90854-2
- 7. Malinowski, Sz., & Zawadzki, I. (1993). On the surface of clouds. *Journal of the Atmospheric Sciences*, 50(1), 5–13. https://doi.org/10.1175/1520-0469(1993)050%3C0005:OTSOC%3E2.0.CO;2
- 8. Morrison, H., Jeevanjee, N., Lecoanet, D., & Peters, J.M. (2023). What controls the entrainment rate of dry buoyant thermals with varying initial aspect ratio? *Journal of the Atmospheric Sciences*, 80(11), 2711–2728. https://doi.org/10.1175/JAS-D-23-0063.1
- 9. Nitsche, M., & Krasny, R. (1994). A numerical study of vortex ring formation at the edge of a circular tube. *Journal of Fluid Mechanics*, 276, 139–161. https://doi.org/10.1017/S0022112094002508
- 10. Sherwood, S.C., Hernández-Deckers, D., Colin, M., & Robinson, F. (2013). Slippery thermals and the cumulus entrainment paradox. *Journal of the Atmospheric Sciences*, 70(8), 2426–2442. https://doi.org/10.1175/JAS-D-12-0220.1
- 11. Shub, M. (2005). What is ...a horseshoe?. Notices of the American Mathematical Society, 52(5), 516–517. https://www.ams.org/notices/200505/what-is.pdf
- 12. Sohn, S.-I. (2014). Two vortex-blob regularization models for vortex sheet motion. *Physics of Fluids*, 26(4), Article 044105. https://doi.org/10.1063/1.4872027
- 13. Vallis, G.K. (2017). Atmospheric and oceanic fluid dynamics. Fundamentals and large-scale circulation (2nd ed.). Cambridge University Press. https://doi.org/10.1017/9781107588417
- 14. Yano, J.-I. (2023). Geophysical convection dynamics. Elsevier.
- 15. Yano, J.-I., & Morrison, H. (2024). Thermal vortex ring: Vortex-dynamics analysis of a high-resolution simulation. *Journal of Fluid Mechanics*, 991, A18. https://doi.org/10.1017/jfm.2024.485

Manuscript received November 30, 2024; accepted for publication July 31, 2025; published online November 7, 2025.